5 Pattern formation during periodate reduction on a Au(111) film electrode in the presence of camphor

5.1 Introduction

In chapter 4 it was demonstrated that the Au(111)/camphor, IO_4^- system possesses an S-shaped current–potential curve. The present chapter deals with pattern formation studies in this system, whereby the focus is on the experimental confirmation of the existence of Turing structures in S-NDR systems as theoretically predicted [28]. Since the theoretical studies predict characteristic changes of global quantities as a function of the resistivity of the electrolyte, which manifets itself also in CVs, we discuss in section 5.1.1 the cyclic voltammetry in different base electrolyte concentrations and rationalize the observed changes. In section 5.1.2, spatially resolved measurements under various experimental conditions are presented, which are compared with the theoretical predictions in section 5.2.

5.2 Results

5.2.1 Global dynamics

The qualitative appearance of the cyclic voltammograms depended strongly on the conductivity of the electrolyte.

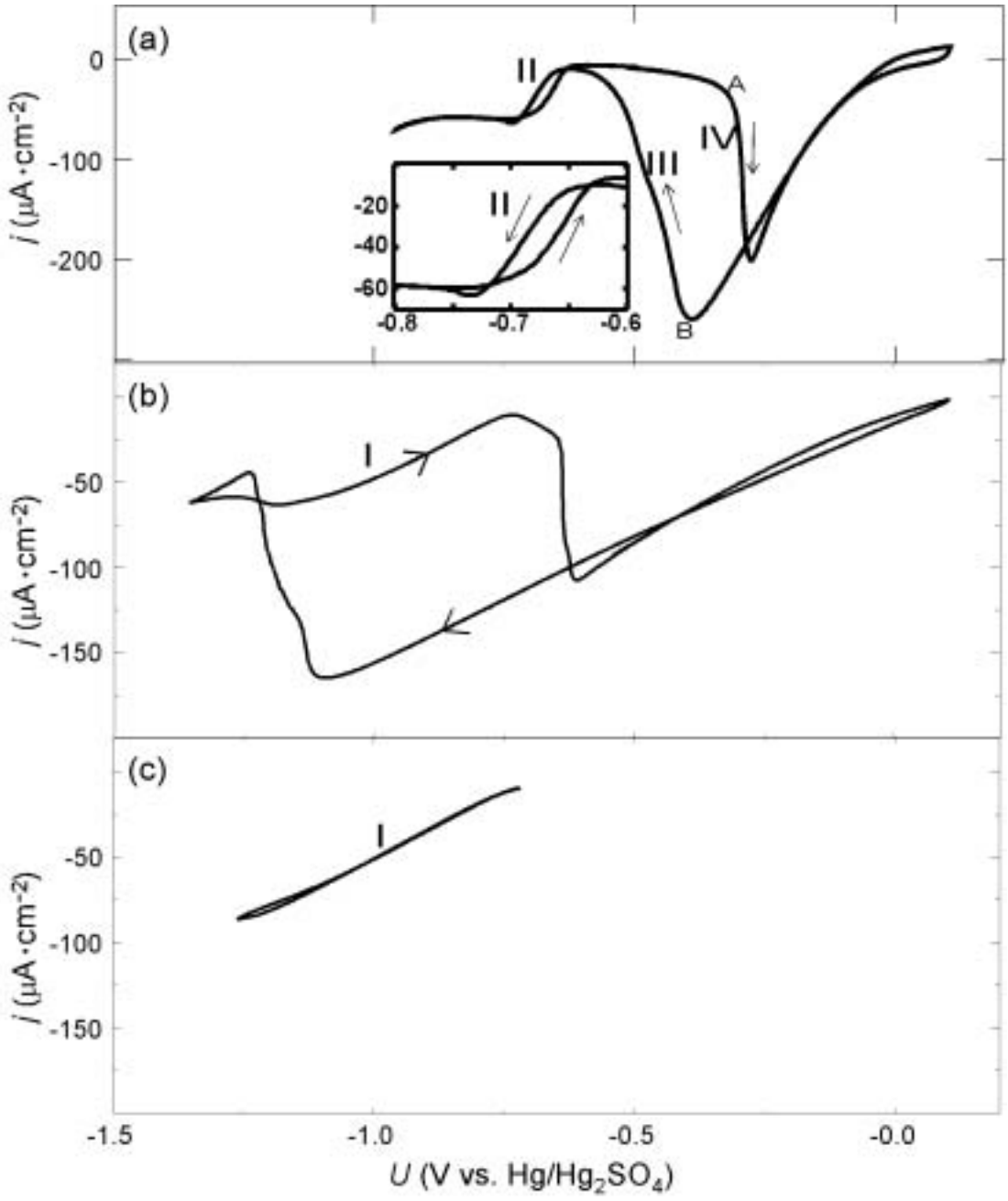

Figure 5.1: *Cyclic voltammograms of the Au/camphor, IO_4^- system for different concentrations of the supporting electrolyte. Electrode: rectangular Au film (30×8 cm^2). Electrolyte : 5 mM camphor, 2 mM $NaIO_4$ and (a) 32 mM $NaClO_4$, (b) and (c) 1 mM $NaClO_4$.*

A CV that is typical for medium and high conductivity of the electrolyte is shown in Fig. 5.1a. Its characteristic features are two regions of the applied

voltage with a hysteresis. One occurs around -0.7 V vs. Hg/Hg_2SO_4 and is labeled II in the figure. With an approximate width of 50 mV, it is rather small. This bistable region is exactly the S-region we are interested in. Due to the finite scan rate of the voltage, the S-region is slightly distorted, and the transitions between the stationary states are not as sharp as in a 'quasi-stationary' experiment. As discussed in section 4.2.3, it is closely linked to the two-dimensional phase transition of the camphor phase between the condensed and the gas-like phases. The second hysteresis, which is bordered by the transitions III and IV between a high current and a passive state and vice versa, also results from a phase transition, which goes along with the replacement of IO_4^- by camphor. As for region II, it is the signature of a bistability, which is observed for zero scan rate. Connecting the ends of the low and high current branches, which are indicated by A and B in Fig. 5.1a, it becomes apparent that the current–voltage characteristic traces out the form of a 'Z'. Thus, the CV exhibits an S-type bistability in the negative potential region and a Z-type bistability at more positive potentials.

Fig. 5.1b shows a CV in a more extended voltage interval for a system with a lower electrolyte conductivity than that of Fig. 5.1a, but otherwise identical concentrations. Clearly, in this case, just one though very broad hysteresis, extending over nearly 500 mV, exists. This broad hysteresis remains also for zero scan rate, confirming that the system is bistable. In contrast, the small loop that can be seen around the negative turning point is a kinetic phenomenon. The bistability is of the Z-type. A comparison of the two CVs of Figs. 5.1a and 5.1b suggests that the two distinct bistable regions of Fig. 5.1a have merged: The branch at positive potentials is clearly coincident with the active branch of the 'Z'. The transition from this branch is, however, going to a state with a current density of about 50 $\mu A/cm^2$, a level that coincides with the value of the high-current branch of the S-type hysteresis in Fig.5.1a, rather than with the one of the passive branch of the original 'Z'. When going into positive direction from the negative turning point, the current density monotonically decreases from the high-density value of the 'original 'S' to the low density value. Any sign of the S-type bistability has disappeared at the lower conductivity.

That the S-type bistability can also not be recovered when restricting the external voltage to values negative to the transition point from the passive to the active branch is shown in Fig. 5.1c. At these negative potentials, the CV is single-valued, the current density increasing with increasing overpotential. Any sign of a dynamic instability is absent. Moreover, apparently it is possible to stabilize the system at current densities that lie between the two stable branches of the S-bistability (and also the Z-bistability) and are thus inaccessible at high conductivities.

Lowering the conductivity implies that the '*IR*' drop through the electrolyte is larger; to adjust a certain state, characterized by the electrode potential, ϕ_{DL}, and the current density, *i*, an external voltage *U* has to be applied, i.e., *IR* larger than ϕ_{DL}, where *R* is the cell resistance: $U = \phi_{DL} + IR$. Let us consider how the larger 'IR' drop changes the CV in the S- and Z-region. First consider the S-region (Fig. 5.2a). The potential drop through the electrolyte is large for large current densities, i.e., on the active branch of the 'S'. Thus, to establish a state on this branch, a considerably higher external voltage has to be applied. In constrast, the 'IR' correction on the low-current density branch is negligible. As a consequence, in a cyclic voltammogram the two branches are pulled apart at low conductivity, and thus the bistable region is converted to a monostable, single-valued region at sufficiently high resistivity. Note that in this case also current densities that lie on the sandwiched, unstable branch of the 'S' are accessible. The branch is apparently stabilized. Thus, the single-valued curve in the restricted voltage range CV displayed in Fig. 5.1c solely results from an S-shaped current electrode potential characteristics and the IR drop through the electrolyte.

In the 'Z'-region, things are exactly opposite (Fig. 5.2b). The larger IR drop at higher current densities leads to a broader hysteresis, thus enlarging the bistable region. In Fig. 5.1b the conductivity is so low that the active branch of the Z reaches values, at which it coexists with the active branch of the 'S'; as a consequence, the CV displays only one bistable region, with the stretched 'S' being part of the passive branch.

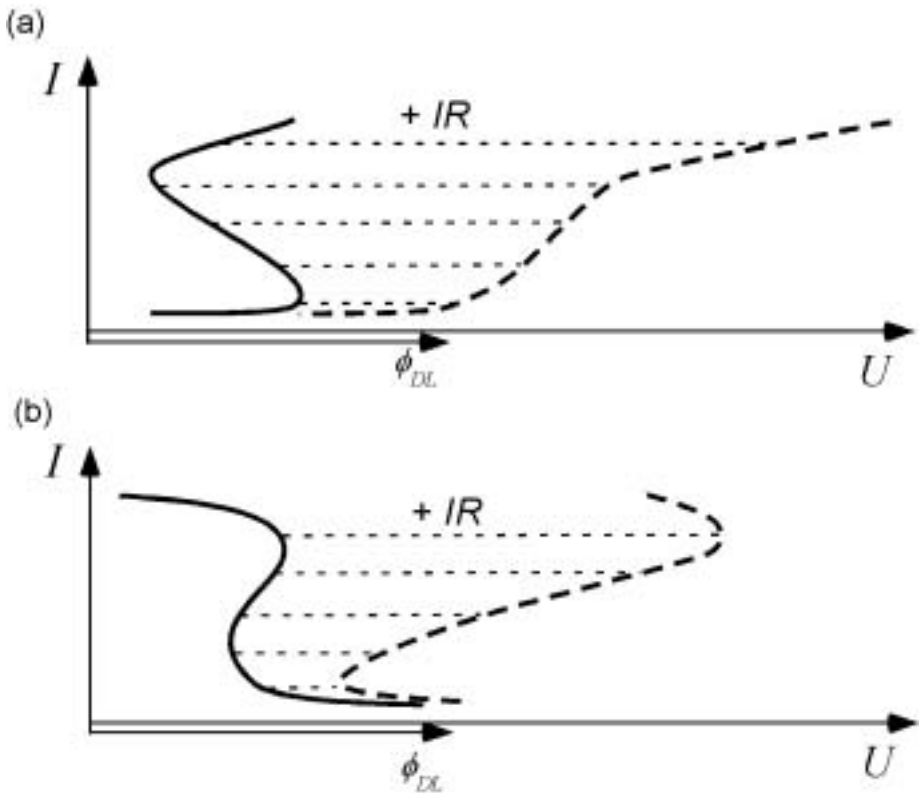

Figure 5.2: *Schematic illustrations of the conductivity effect: (a) An 'S' shaped current–double layer potential curve is changed to single-valued current–external potential curve for a large enough electrolyte resistance, i.e., a sufficiently low conductivity. (b), In the case of a 'Z' shaped current–double layer potential curve, in a CV the bistable region becomes the broader the lower the conductivity.*

5.2.2 Spatially resolved measurements: SPI studies

a) Small disk electrode

The studies on pattern formation were first carried out with the smaller disk electrodes which had a diameter of 6 mm. The initial search for patterns was carried out during potential scans. Thereby it turned out that whenever the conductivity was so small that the current–voltage curve was single-valued, a spot-like region appeared in the voltage region which corresponded to intermediate current densities that are not accessible at high conductivity. A typical experiment is shown in Fig. 5.3 and Fig. 5.4.

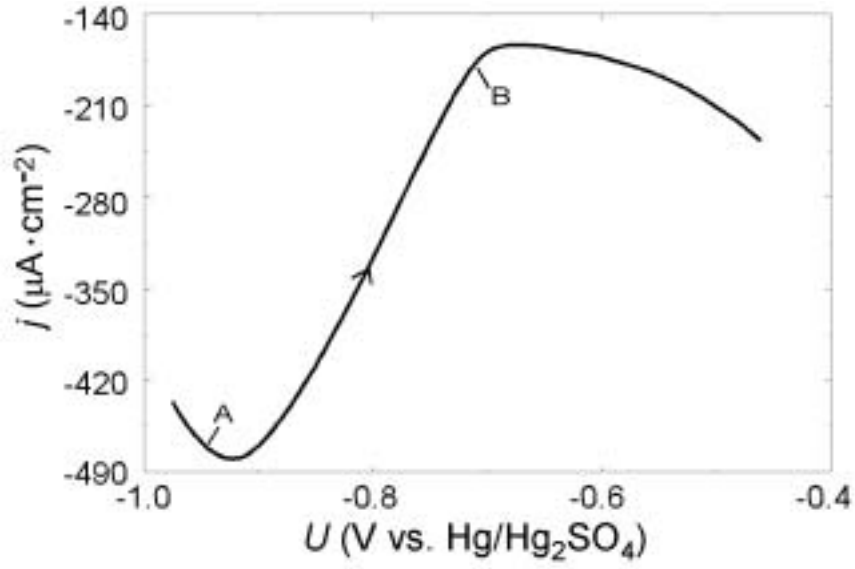

Figure 5.3: *Current–potential curve in the S region. Scan rate: 50 mV/s, 5 mM camphor, 10 mM $NaIO_4$. The region between A and B corresponds to the potential interval in which the SPR images shown in Fig. 5.4 were recorded.*

Fig. 5.3 shows a current-voltage scan with a scan rate of 50 mV/s, Fig. 5.4 the SPI images that were recorded between the points marked by A and B in Fig. 5.3. Point A corresponds to a state on the active branch of the i/ϕ_{DL} curve. Clearly, at this state the electrode is homogeneous. Furthermore, from SPRA measurements (cf. Fig. 4.9) we know that in the active state the electrode is practically camphor free. Thus, the initial blue image in Fig. 5.4 corresponds to a homogeneous, bare electrode surface. In the second image, a faint reddish-green region appears. This image was recorded at an external voltage of U = -0.925 V, i.e., slightly positive to the minimum of the i/U curve, and thus the corresponding i/ϕ_{DL} value lies on the sandwiched state (cf. Fig. 5.2a).

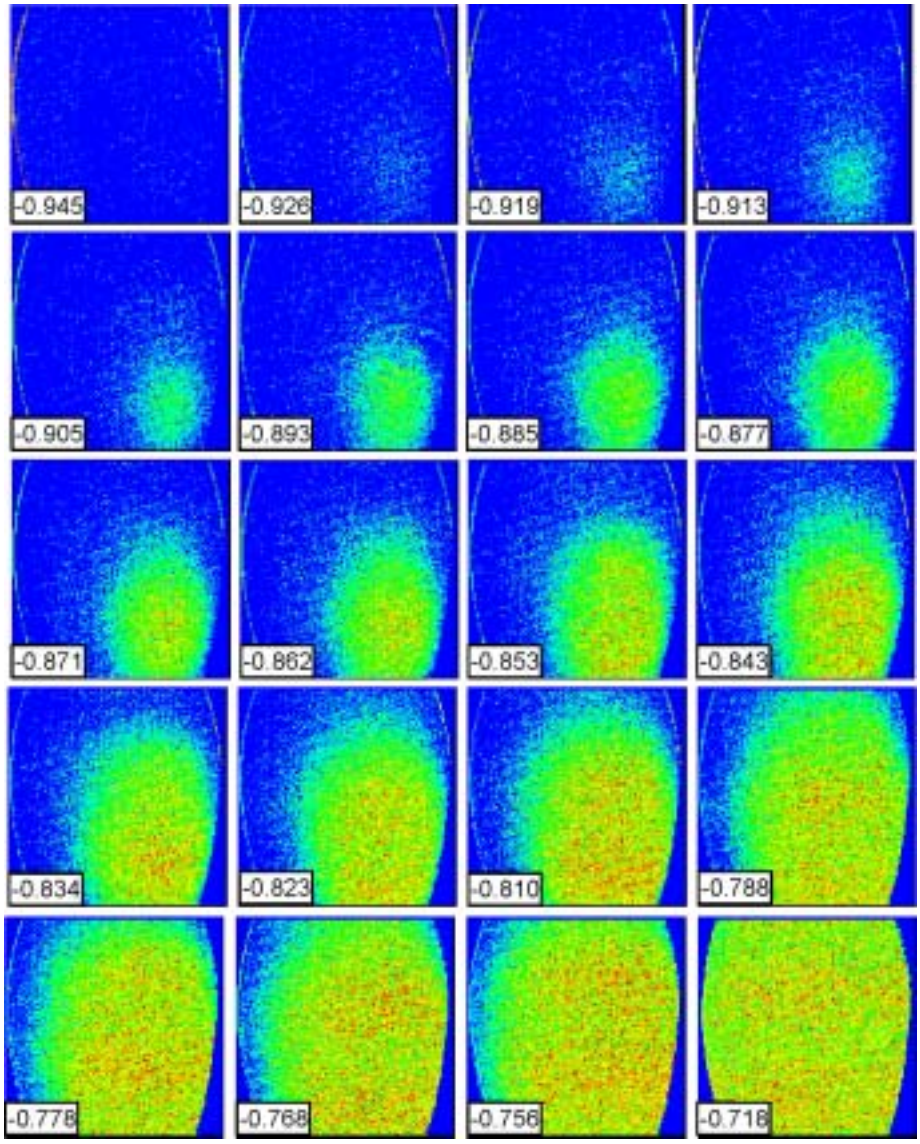

Figure 5.4: *The sequence of images observed during the anodic potential scan in the S region (-0.945 V, -0.718 V) corresponding to the curve between A and B in Fig. 5.3.*

The yellow color indicates that some camphor adsorbed on the electrode. The fact that the color does not change homogeneously over the entire electrode indicates that the camphor film starts to grow locally. The spot becomes more pronounced and grows as the voltage is scanned further into the positive region, until the camphor film covers homogeneously the entire electrode surface at point B.

The interesting question is whether the inhomogeneous growth of the condensed camphor phase is a transient phenomenon or whether the spot-like structure remains stationary when the voltage is kept constant. Because the contrast of the images was rather low, the profile of the laser beam had a Gaussian intensity distribution and was also somewhat disturbed by unavoidable refraction patterns. Since (even though the beam was passed through the coherence scrambler) the coherence could not be destroyed completely (cf. section 3.1.3), it was not possible to obtain a sufficient contrast when a series of images was recorded at constant voltage. To circumvent this problem, the voltage was stepped from a value on the active branch, i.e., from a completely homogeneous state, into the region in which the spots were observed during the scan experiments. In this way, it was ensured that the series of images recorded exhibited an evolution, and the succession of images could be processed as described in section 3.1.3. In these experiments, the spots attained a characteristic size which was constant for the rest of the experiment, suggesting that in fact a stationary structure formed. Note, however, that due to the experimental constraints, the observation time was limited, so that these experiments did not allow to make statements about the long-term stability of the spots.

Further hints that the structured states are indeed stable were obtained from experiments, in which the potential was sinusoidally forced. We hold the potential in the most cathodic region (-1.060 V) first, then jump the potential into the 'S' region (-0.801 V) as well as apply an external sinusoidal potential signal between the WE and RE. The sinusoidal potential is of 1.0 Hz frequency and 70 mV amplitude. The potential program and the corresponding response current as well as the average light intensity recorded by SPI are shown in Fig. 5.5.

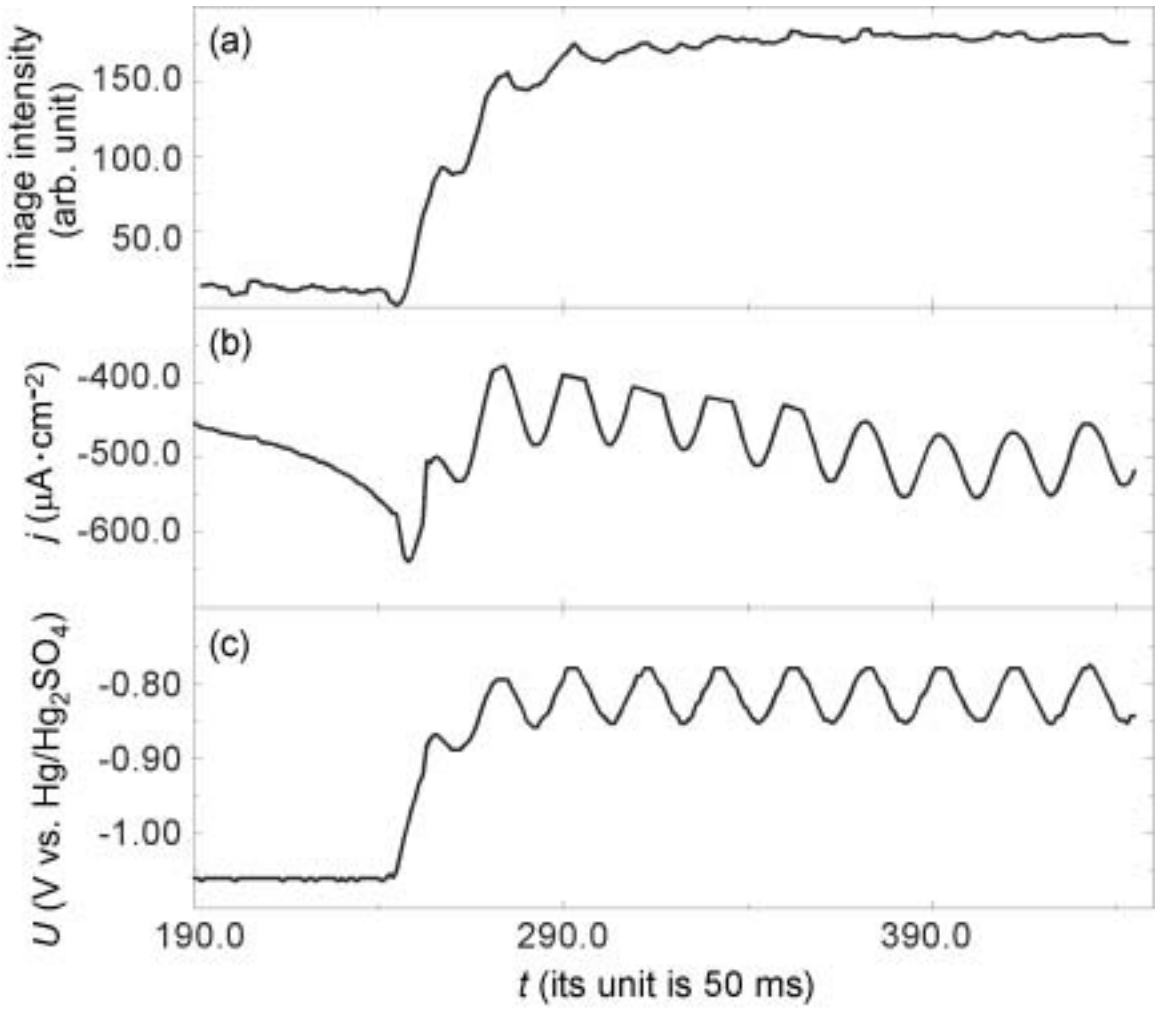

Figure 5.5: *Time series of potential (c), current (b) and average light intensity in SPI (a) before and after (t = 243) jumping the potential to -0.801 V as well as adding an external sinusoidal potential signal (frequency 1.0 Hz, amplitude 70 mV).*

We can see from Fig. 5.5 that the potential jump practically does not give rise to a sharp transition due to the limitation of the potentiostat. In our case, the potential change rate is about 200 mV/s during the potential jump. After the addition of the external sinusoidal potential signal, the potential between WE and CE, the current density on WE and the average light intensity were all modulated by the external potential perturbation and gave out the corresponding responses.

Although the average light density on Fig. 5.5 did not reveal regular oscillations as the potential and current density curves did, we could still see that it responded to the potential perturbation in the same period, though with a certain small delay.

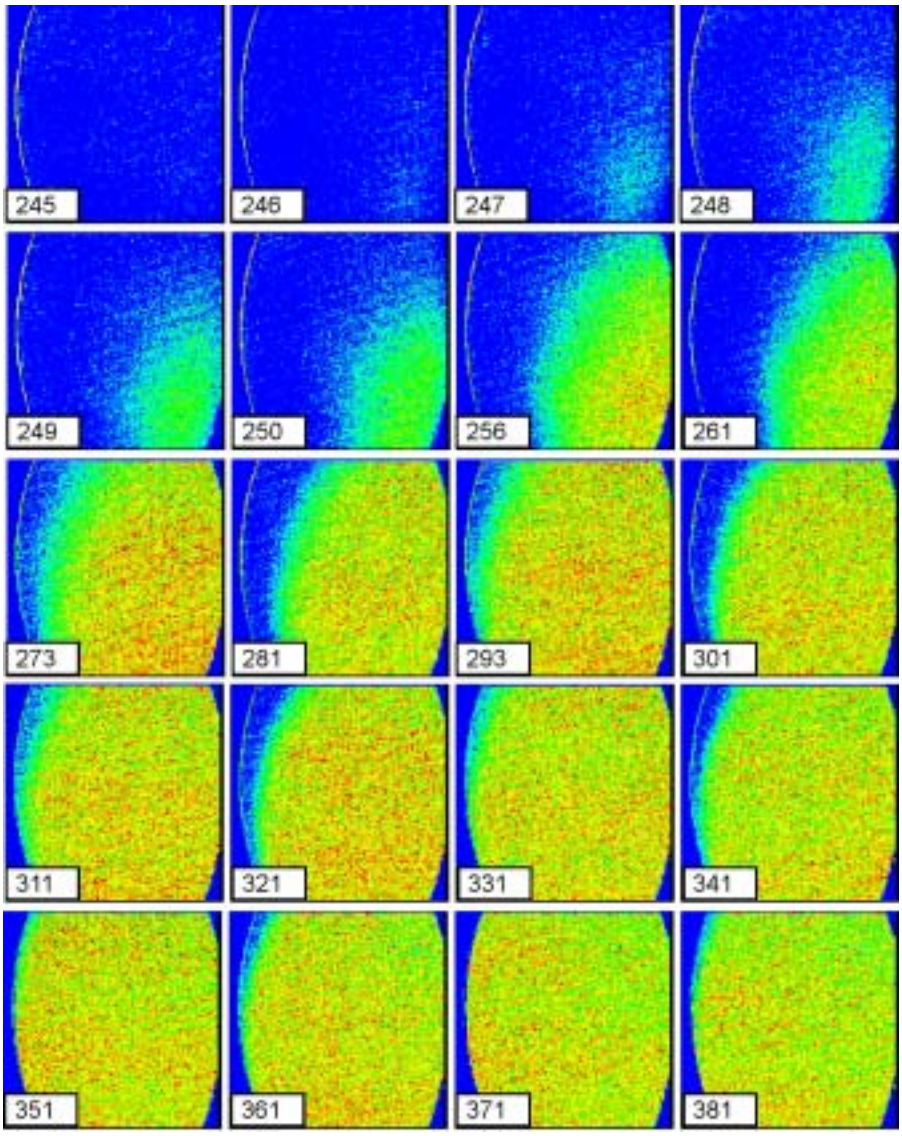

Figure 5.6: *Perturbation effect by sinusoid potential signal (1.00 Hz in frequency and 70 mV in amplitude).*

From the image series recorded by SPI in Fig 5.6, we observed the spatial patterns modulated by the external sinusoidal potential perturbation.

The size of the spots oscillated with the same frequency as the applied potential. This is a strong hint that at more negative potentials smaller spots are more stable than at more positive potentials, suggesting again that stationary spots indeed exist along the sandwiched branch of the 'S' at low conductivity.

According to the above mentioned theoretical predictions, Turing structures should exist in the parameter region in which the stationary spots were observed. Turing structures are stationary patterns which possess an intrinsic wavelength. Obviously, as long as only one spot is observed, it is not possible to determine a wavelength. For this reason, experiments were carried out with larger electrodes.

b. Rectangular Au(111) film electrode

When employing rectangular film electrodes of 30×8 mm^2, indeed, stationary structures with a different number of spots were observed, depending on the composition of the electrolyte. Examples of experiments in which one, two or three spots were obtained are displayed in Fig. 5.7a-c. The individual images within one series correspond to different values of the applied external voltage, each series being obtained at different concentrations of supporting electrolyte ($NaClO_4$) and/or periodate. In the case of two and three spots, it is possible to assign a wavelength to the patterns. Obviously, the wavelength depends on the system's parameters, as it is the characteristic for Turing patterns.

While each sequence of images displayed in Fig. 5.4 was obtained during a slow potential scan, much care was taken to confirm that the patterns remain stationary at a given value of the applied voltage. The protocol employed to ensure the stationarity of the structures is shown in Fig. 5.8. First, a sequence of images was recorded during a voltage scan. The scan was stopped at some value within the pattern forming region. Then the system was kept at this value for at least 5 minutes. Finally, another sequence of images was recorded, starting at this value of the externally applied voltage and sweeping the voltage either into the cathodic or the anodic direction. Only when the final image of the first series and the first image of the last series did not show apparent differences, the pattern was classified as a stationary pattern.

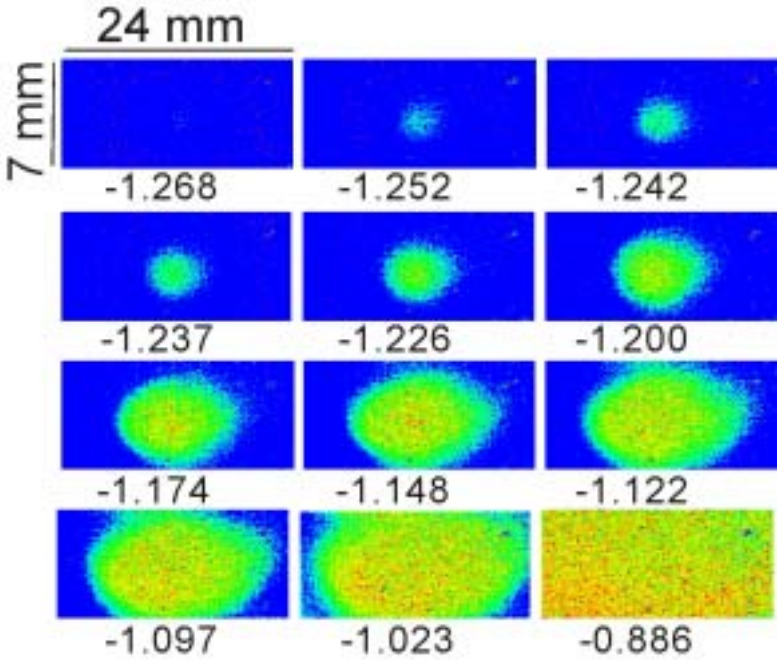
24 mm
7 mm
-1.268
-1.252
-1.242
-1.237
-1.226
-1.200
-1.174
-1.148
-1.122
-1.097
-1.023
-0.886

(a)

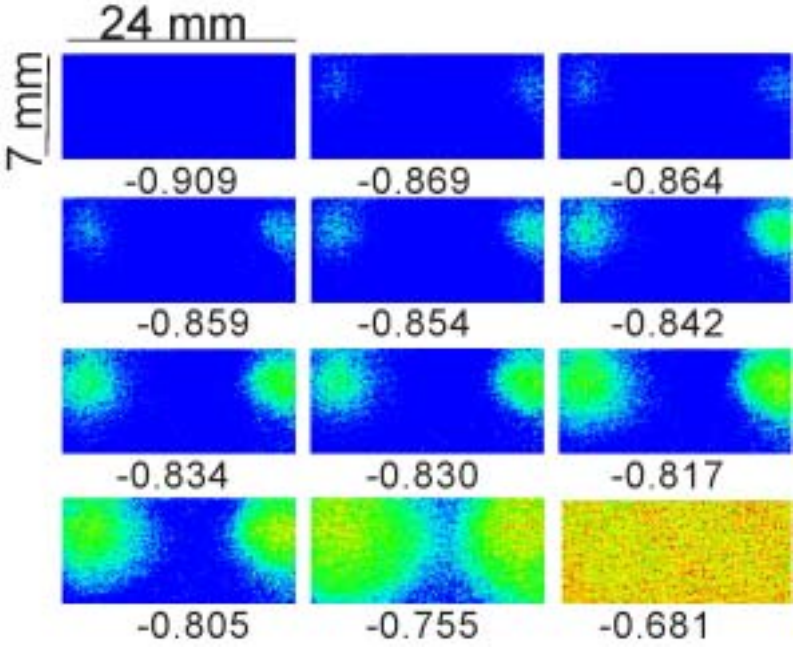
24 mm
7 mm
-0.909
-0.869
-0.864
-0.859
-0.854
-0.842
-0.834
-0.830
-0.817
-0.805
-0.755
-0.681

(b)

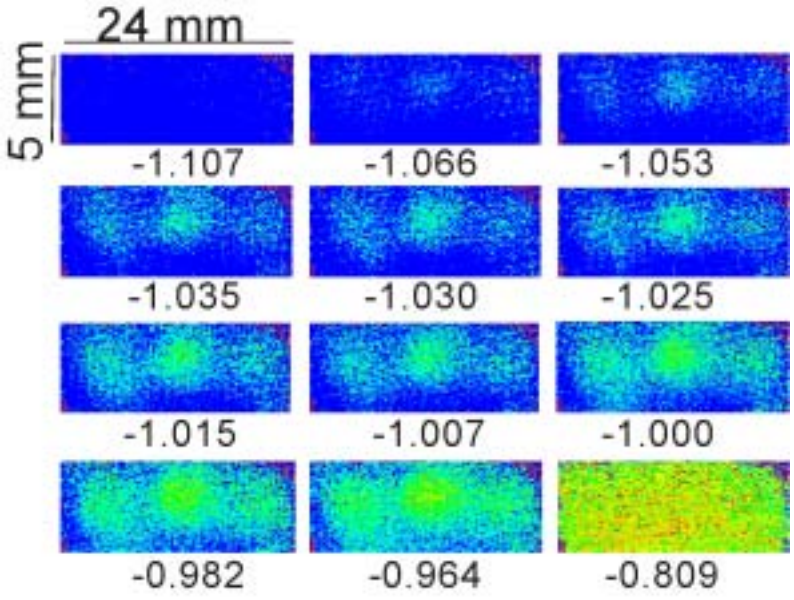

(c)

Figure 5.7: Patterns emerging in different electrolyte compositions (scan rate 50 mV/s). (a) 5 mM camphor, 0.5 mM $NaClO_4$, 0.5 mM $NaIO_4$. (b) 5 mM camphor, 1 mM $NaClO_4$, 1 mM $NaIO_4$; (c) 5 mM camphor, 0 mM $NaClO_4$, 1 mM $NaIO_4$.

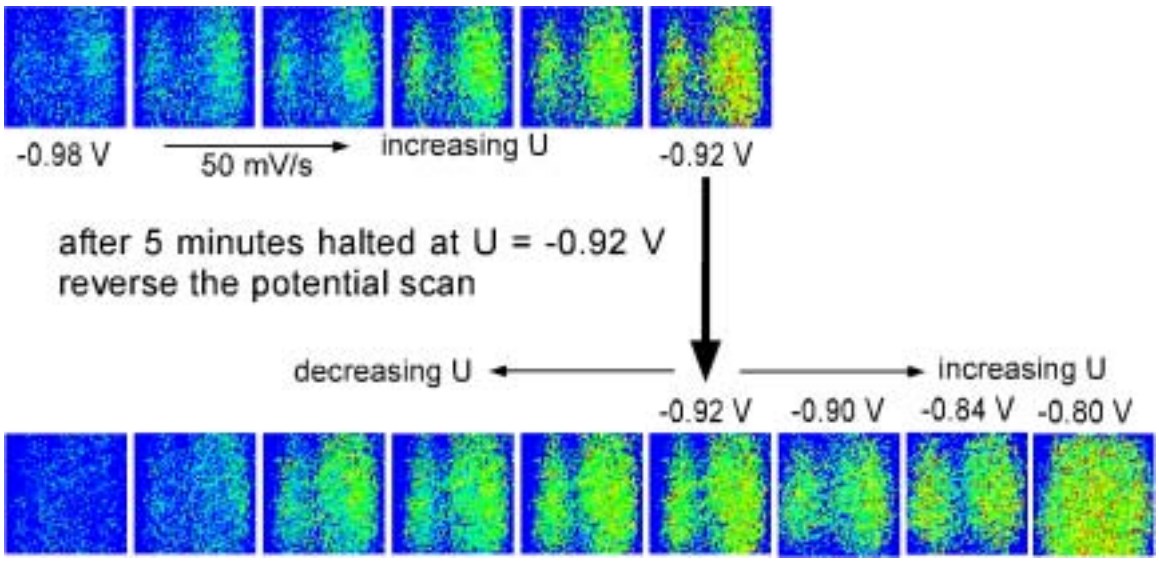

Figure 5.8: Test for the stationarity of observed patterns in the 'S'-region. The voltage was scanned to the desired value, where it was kept constant for 5 minutes. After this time the voltage scan was reversed. Images were taken during the forward scan and the initial 'holding time' (first series) and at the last phase of the holding time and during the reverse scan (electrode: Au(111) film (30 mm×8 mm)).

Stationary patterns were obtained—independent of the periodate concentration—whenever the total conductivity was low enough such that the CV exhibited a single-valued curve. The existence region of stationary patterns in the parameter plane spanned by the external voltage and the resistivity of the electrolyte is shown in Fig. 5.9. It is V-shaped and opens towards larger resistivity and larger overvoltage. Bistable behavior existed only for an electrolyte resistivity below the tip of the 'V'.

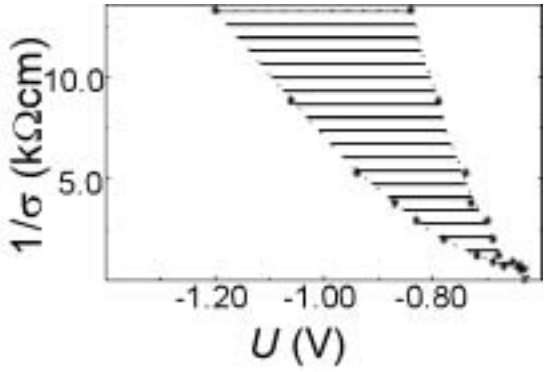

Figure 5.9: Existence region of the patterns in the electrolyte resistance vs. external voltage plane (from the experimental results). The electrolyte resistance, $1/\sigma$*, was calculated from the ionic concentrations* c_i *according to* $\sigma = \left(\frac{FD}{RT}\right)\sum_i \left(n_i^2 c_i\right)$*; F: Faraday's constant, D:* 10^{-5} *cm²/s, R: gas constant, T: absolute temperature,* n_i*: charge number of the ionic species i,* c_i*: concentration of the ionic species; i:* Na^+*,* IO_4^-*,* ClO_4^-*. Electrolytes: 5 mM camphor, 0.5 mM* $NaIO_4$*, x mM* $NaClO_4$*.*

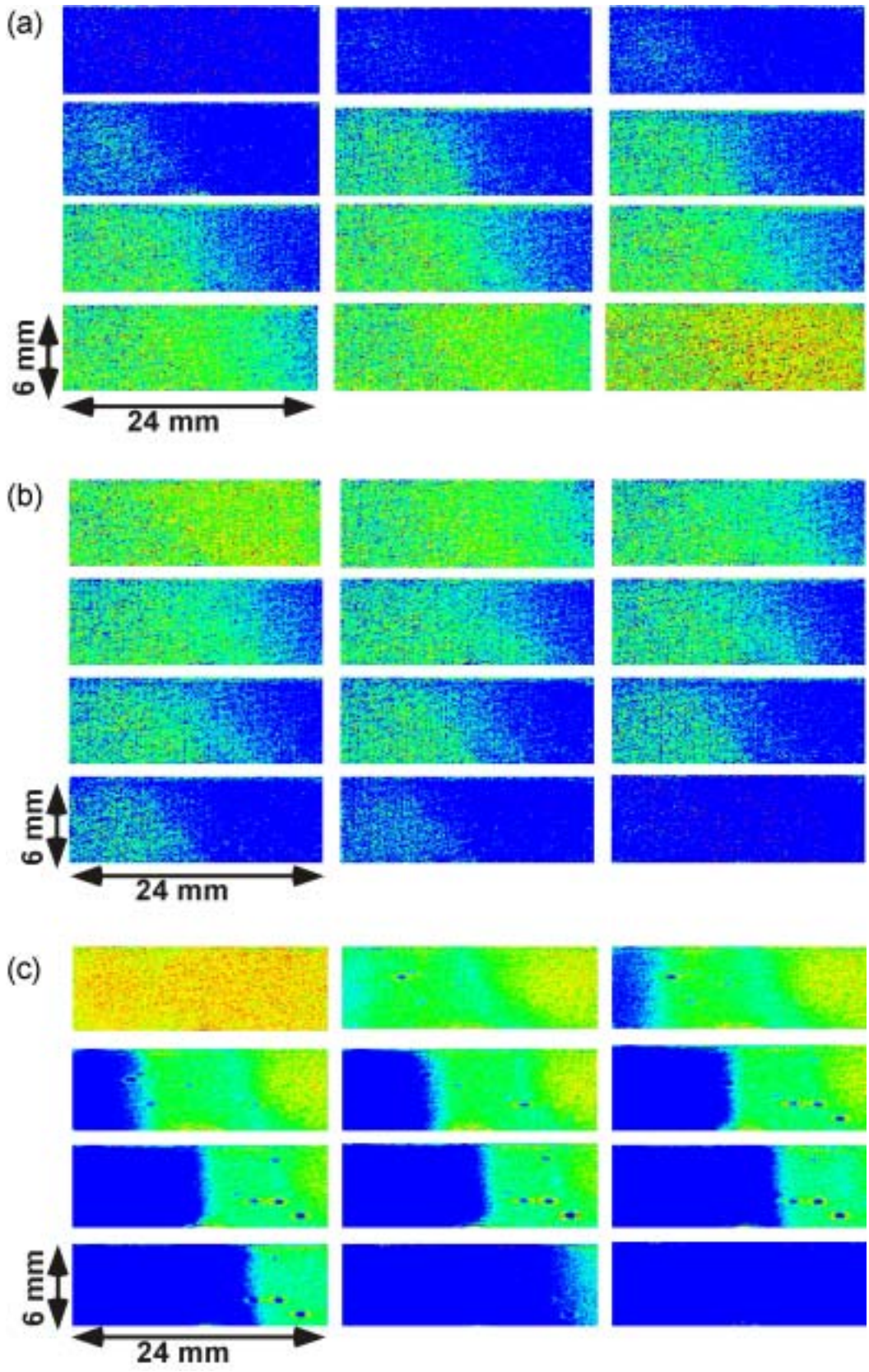
(a)
6 mm
24 mm
(b)
6 mm
24 mm
(c)
6 mm
24 mm

Figure 5.10: Waves in different regions: (a) region II; (b) region IV; (c) region III. The common conditions are: 5 mM camphor, 1 mM $NaIO_4$, 32 mM $NaClO_4$, scan rate 50 mV/s.

A transition from the active to the passive branch of the 'S' within the bistable region is shown in Fig. 5.10a. Again the transition did not occur homogeneously over the entire electrode. Instead, the condensed camphor layer nucleated close to one of the smaller sides of the rectangular electrode and spread fast to the edges of this side, then to propagate as a plane wave from one end to the other one. Such a propagating wave or traveling front is characteristic for transitions in the bistable regime. In our context, it is noteworthy that these fronts in the bistable region never nucleated at the positions at which the 'low current spots' occurred for lower conductivity. This is another confirmation that the position of the spots is not determined by defects on the electrode.

Also the transitions between the different states in the 'Z' region were accompanied by fronts. A transition from the camphor covered state to the active state is displayed in Fig. 5.10b. This transition corresponds to transition III in Fig. 5.2a. (Note that the small spots on the images are optical artifacts; they are neither related to self-organization phenomena nor to defects on the Au film.)
Again, the front formed close to a smaller side of the rectangular electrode and propagated across it from one end to the other. As in the case of the active/ passive transition in the 'S'-region, the fronts were broad and somewhat smeared out. This was different for the transitions from the active 'Z'-state to the active 'S'-state (cf. transition IV in Fig. 5.2a). As can be seen in Fig. 5.10c, the interfaces connecting different phases represent sharp boundaries. Moreover, most strikingly, there are not two distinct phases as for the transitions discussed so far but three. Above we argued that in the periodate, camphor/Au(111) system the electrode is covered by a periodate adlayer in the positive potential region. At more negative potentials, the periodate adlayer is replaced by a condensed camphor film. At even more negative potentials, camphor desorbs leaving a nearly bare Au electrode (cf. Fig. 4.9). At high resistivity, as it was the case when Fig. 5.10c or Fig. 5.2a were recorded, we discussed that the transition from the active branch of the Z goes to the active branch of the S. In the transition region, however, the electrode potential varies monotonically from values, at which the periodate adlayer is stable, to values, at which the Au electrode is nearly

adsorbate free, and thus attaining also values at which camphor adsorbs in a condensed phase. The three different intensity levels seen during the transition in Fig. 5.10c can be attributed to the periodate covered phase (red), which is the metastable active state (first image), the camphor covered state (yellow) and the bare Au electrode (blue), which is the stable low-current state (last image). This front is thus one of the rare examples, in which the interfacial region contains a third phase. Finally, it should be noted that within the 'Z'-region for none of the tested conditions stationary patterns could be found. All structures observed were transient phenomena.

5.3 Discussion

As discussed above, the camphor,periodate/Au(111) system possesses stationary patterns which for sufficiently large electrodes possess an intrinsic wavelength, i.e., a wavelength which depends only on the system's parameters, such as rate constants, concentration of the reactive species or conductivity, but not the geometrical extensions of the electrode. These patterns exist exclusively around a state in the CV that is transformed in the *unstable* saddle point of an S-type bistability at higher conductivity. Under all other conditions, the long term behavior was found to be homogeneous, while transitions in the bistable regions were accompanied by fronts. These are exactly the features that were theoretically predicted. Moreover, the theoretical analysis showed that the stationary patterns emerge due to local activation and long-range inhibition, as do Turing patterns, and can, in fact, be classified as Turing-type patterns [28]. The experimental results presented above thus represent the first example of electrochemical Turing patterns. In the following, the formation of the Turing patterns is rationalized, partly using theoretical results discussed in [28, 87].

Let us first consider the dynamics of the homogeneous (i.e., only time-dependent) system. If one starts with a camphor containing solution at a negative potential (e.g., close to the negative turning point), an increase of the potential to more positive values causes an increase of the equilibrium concentration of adsorbed camphor. The rise in coverage continues, until at a critical coverage, a first-order phase transition to a dense film with high camphor concentration takes place,

due to the operation of attractive interactions between the adsorbates. Thus, reduction of IO_4^- will be inhibited causing a decrease of the current density *I*. Under potentiostatic conditions, this inhibition prompts a shift of ϕ_{DL} toward more cathodic (i.e., negative) values. Camphor will now desorb more readily, and a negative feedback loop is created: Because the build-up of the camphor film is associated with a decrease of the current density for periodate reduction, the response of the system (through the double layer potential) limits the growth of the camphor film. Thus, our system represents an activator/inhibitor system, whereby the camphor coverage takes the role of the activator and the electrode potential of the inhibitor. That the dynamics of a system follows an activator/inhibitor-type dynamics is the first prerequisite for the existence of Turing patterns.

A general model for description of the spatiotemporal self-organization in such systems may be written with two equations [28]. Eq. (5.1) extends the homogeneous (i.e., local) dynamics of the concentration θ of the activator ($\hat{=}$ camphor coverage) as described by the function $f(\theta, \phi_{DL})$ to spatial spreading via diffusion as characterized by the diffusion constant *D*:

$$\frac{\partial \theta}{\partial t} = f(\theta, \phi_{DL}) + D\nabla^2\theta \ . \tag{5.1}$$

Eq. (5.2) is the central expression for pattern formation in electrochemical systems, which follows from local charge balance [88]:

$$C\frac{\partial \phi_{DL}}{\partial t} = g(\phi_{DL}, \theta) - \sigma\left(\left.\frac{\partial \phi}{\partial z}\right|_{z=WE} - \frac{U-\phi_{DL}}{\beta}\right), \tag{5.2}$$

where *C* is the specific double layer capacitance, σ the specific conductivity of the electrolyte, which together with the geometric factor β determines the cell resistance per unit electrode area. *U* is the externally applied voltage, $U - \phi_{DL}$ the electric potential in the electrolyte, and *z* the coordinate normal to the electrode.

In analogy to reaction–diffusion equations, the local dynamics of the electrochemical system is comprised in the function $g(\phi_{DL}, \theta)$, and the second term on the right hand side of Eq. (5.2) is the counterpart to the diffusion term in Eq. (5.1); it represents spatial coupling between different locations on the electrode due to an inhomogeneous potential distribution. Diffusion is thus replaced by migration.

The key element for spontaneous spatial symmetry breaking in an activator–inhibitor system is the ratio of the characteristic rates of the transport processes associated with the activator and inhibitor variables. This rate determines the effective ranges of the respective influence. For the sake of simplicity, consider a onedimensional (1D) electrode of length L. Then, the ratio of the rate of migration and diffusion is given by a dimensionless constant $d \propto (L\sigma)/(D\,C)\,L$, σ and C are readily accessible. Taking 10^{-5} cm^2/s as an upper boundary for D and typical values for the other three parameters, d results to be on the order of 10^3 to 10^4. Thus, the potential spreads by far faster than the coverage does. This is exactly the situation that leads to a destabilization of the homogeneous state and thus to the formation of patterns. For a 1D electrode with periodic boundary conditions, model Eqs. 5.1 and 5.2 possess stationary periodic solutions [28]. They bifurcate from the homogeneous state, and their wavelength depends solely on the rate constants of the model (and not on the size of the electrode as one might conjecture because it enters the parameter d [28]. Thus, the patterns have all of the characteristics of Turing patterns. Plotting the location of the calculated Turingtype instability in the σ^{-1}/U parameter plane, a similar V-shaped region (Fig. 5.11) is obtained as in the experiment (Fig. 5.9) (despite the different electrode geometry).

The fact that the experimental results match nearly 1:1 the theoretical predictions is not only a strong support that the observed stationary structures are indeed Turing structures. It also presents evidence that electrochemical Turing structures indeed exist in all electrochemical systems that possess an S-shaped current–potential curve. This realization is especially important since in the pattern forming region the global signal (e.g., the current–voltage curve) does not exhibit any sign of a dynamic instability.

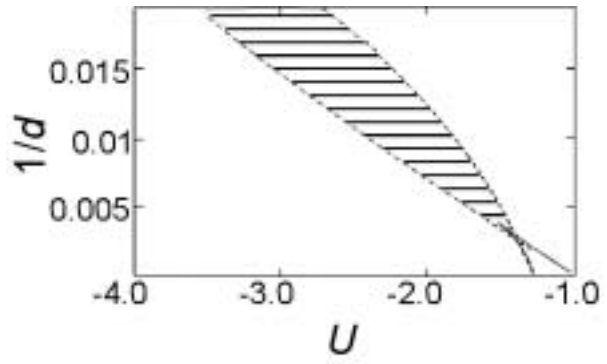

Figure 5.15: *Existence region of the patterns in the electrolyte resistance vs. external voltage plane. Theoretical diagram: The diagram was calculated with the dimensionless version of Eqs. (5.1) and (5.2)* $\frac{\partial\theta}{\partial t} = \mu\, \mathrm{f}(\theta,\phi_{DL}) + \frac{\partial^2\theta}{\partial x^2}$, $\frac{\partial\phi_{DL}}{\partial t} = \mathrm{g}(\theta,\phi_{DL}) - \frac{d}{\beta}\left(\left.\frac{\partial\phi}{\partial z}\right|_{z=-1} - (U-\phi_{DL})\right)$, *where* $\mathrm{f}(\theta,\phi_{DL}) = (1-\theta)\mathrm{e}^{-0.025\phi_{DL}^2+2.4\theta} - 0.5\theta\mathrm{e}^{+0.025\phi_{DL}^2-2.4\theta}$, $\mathrm{g}(\theta,\phi_{DL}) = \kappa(1-\theta)\mathrm{e}^{\phi_{DL}} + \frac{d}{\beta}(U-\phi_{DL})$, μ *= 25,* κ *= 10,* β *= 10. z = -1 is the boundary between electrolyte and electrode.* $\frac{\partial\phi}{\partial z}$ *was obtained from the solution of Laplace's equation* $\Delta\phi = 0$*, subject to periodic boundary conditions in x (parallel to the one-dimensional electrode), and to* $\phi(x,t,z=0) = 0$, $\phi(x,t,z=-1) = \phi^0$, $U = \phi_{DL}(x) + \left.\phi(x)\right|_{z=-1}$. *(Laplace's equation governs the potential distribution in the electrolyte. The electrolyte was assumed to be two-dimensional, z = 0 being the end of the domain opposite to the WE.) The physical quantity* $1/\sigma$ *was recalculated from d =* $(L\sigma)/(2\pi DC)$ *with L = 1 cm, D =* 10^{-5} cm^2/s*, C = 10* μ *F/* cm^2*. U is given with respect to the point of zero charge.*

5.4 Summary

Experimental stationary patterns with an intrinsic wavelength were presented in a system which possesses an S-type bistability. The patterns existed in parameter regions in which the S was stretched to a single-valued current–external potential characteristics. A comparison with existing theoretical predictions confirmed that the observed patterns are Turing-type structures.

Thus, it could be verified that a new kind of Turing-type structures can arise in electrochemical systems with a certain current–potential characteristics. This

finding may open prospects toward the tailoring of patterned electrodes. Furthermore, it remains to be examined whether the same mechanism is responsible for some structure formation phenomena in a biological environment, where potential gradients exist.